Draft version November 4, 2021
Typeset using LaTeX **twocolumn** style in AASTeX63

Assessing the Impact of Hydrogen Absorption on the Characteristics of the Galactic Center Excess

Martin Pohl,[1,2] Oscar Macias,[3,4] Phaedra Coleman,[5] and Chris Gordon[5]

[1] *University of Potsdam, Institute of Physics and Astronomy, D-14476 Potsdam, Germany*
[2] *Deutsches Elektronen-Synchrotron DESY, Platanenallee 6, 15738 Zeuthen, Germany*
[3] *GRAPPA − Gravitational and Astroparticle Physics Amsterdam, University of Amsterdam, Science Park 904, 1098 XH Amsterdam, The Netherlands*
[4] *Institute for Theoretical Physics Amsterdam and Delta Institute for Theoretical Physics, University of Amsterdam, Science Park 904, 1098 XH Amsterdam, The Netherlands*
[5] *School of Physical and Chemical Sciences, University of Canterbury, Christchurch, New Zealand*

Submitted to ApJ

ABSTRACT

We present a new reconstruction of the distribution of atomic hydrogen in the inner Galaxy that is based on explicit radiation-transport modelling of line and continuum emission and a gas-flow model in the barred Galaxy that provides distance resolution for lines of sight toward the Galactic Center. The main benefits of the new gas model are, a), the ability to reproduce the negative line signals seen with the H*I*4PI survey and, b), the accounting for gas that primarily manifests itself through absorption.

We apply the new model of Galactic atomic hydrogen to an analysis of the diffuse gamma-ray emission from the inner Galaxy, for which an excess at a few GeV was reported that may be related to dark matter. We find with high significance an improved fit to the diffuse gamma-ray emission observed with the *Fermi*-LAT, if our new H*I* model is used to estimate the cosmic-ray induced diffuse gamma-ray emission. The fit still requires a nuclear bulge at high significance. Once this is included there is no evidence for a dark-matter signal, be it cuspy or cored. But an additional so-called boxy bulge is still favoured by the data. This finding is robust under the variation of various parameters, for example the excitation temperature of atomic hydrogen, and a number of tests for systematic issues.

Keywords: Gamma-ray astronomy — dark matter — Galactic center

1. INTRODUCTION

Since its discovery some ten years ago (Hooper & Goodenough 2011), the excess of gamma rays observed with the Fermi-LAT from the Galactic-center region (GCE) has remained one of the most intriguing open questions in astroparticle physics. Although published interpretations concentrate on a dark-matter interpretation or a millisecond pulsar related origin, there is no consensus on the origin of this so-called Galactic-center excess (e.g., Gordon & Macías 2013; Macias & Gordon 2014; Abazajian et al. 2014; Ackermann et al. 2017; Macias et al. 2018; Bartels et al. 2018; Macias et al. 2019; Abazajian et al. 2020; Di Mauro 2021). One of the main systematic difficulties is the need to accurately model the intense diffuse gamma-ray emission and the gamma-ray sources in the region.

Several studies have claimed to find a non-Poissonian component to the GCE (Bartels et al. 2016; Lee et al. 2016), which may be further evidence for the millisecond-pulsar explanation. However, there is some controversy regarding the level of systematics in this approach (e.g., Leane & Slatyer 2019, 2020a,b; Buschmann et al. 2020a; Chang et al. 2020; Calore et al. 2021; List et al. 2021; Mishra-Sharma & Cranmer 2021).

Modelling the diffuse interstellar gamma-ray emission requires knowledge of the distribution of gas in the Galaxy, which must be convolved with the spatial distribution of cosmic rays to estimate the gamma-ray emissivity along each line of sight. Line spectra of atomic hydrogen and other tracer elements or molecules provide information on the line-of-sight velocity of the gas, whereas what is needed is the distribution along the line of sight. Pohl et al. (2008) used a gas-flow model based on the smoothed particle hydrodynamic (SPH) simulations described in Bissantz et al. (2003) to deconvolve CO data. They employed an iterative method to successively reduce signal in the line spectrum and place it at the eight best-matching distance intervals,

until there is only noise left. In Macias et al. (2018) an analogous deconvolution of H*I* data was found to provide a better fit to the diffuse gamma-ray emission from the Galactic-center region than do the gas maps of the standard *Fermi*-LAT data analysis pipeline[1] (see also Jóhannesson et al. 2018a). The absorption correction was minimal and involved only self-absorption with constant excitation temperature $T_{\rm exc} = 170\,{\rm K}$. Continuum emission was ignored, which means weak positive signal was deemed optically thin and negative signal had to be disregarded. In the Galactic-center region these simplifications lead to a potentially significant underestimation of the mass of atomic gas, and hence a deficit in the predicted diffuse gamma-ray emission and an artificial indication for new emission components.

In this paper we present an advanced model of atomic gas in the Galaxy and apply it to the analysis of gamma-ray emission from the Galactic center. We account for both line and continuum emission in the radiation transport, which allows the modelling of negative line intensity and traces gas in both emission and absorption. We find good fits for a broad range of excitation temperatures, $T_{\rm exc} \gtrsim 180\,{\rm K}$, in good agreement with the findings of Gibson et al. (2005). For better comparison with the results of Macias et al. (2018) we retained with minor modifications the gas-flow model and rotation curve as used in Pohl et al. (2008), although newer studies of gas flow and Galactic rotation had been published (e.g. Baba et al. 2010; Pettitt et al. 2014; Sofue 2015; Mertsch & Vittino 2020). The recently observed radial flow beyond the solar circle (Chrobáková et al. 2020) should not be relevant for the lines of sight toward the inner Galaxy that we consider here.

2. METHOD

2.1. *Radiation transport*

The radiation transport equation for the intensity, I, along a line of sight, s, reads

$$\frac{dI}{ds} = j_c + j_l - \alpha_l I \ . \tag{1}$$

where we allow for continuum emission with coefficient j_c, line emission, j_l, and absorption, α_l. Continuum absorption is ignored, because the brightness temperature is always very much smaller than the excitation temperature for free-free emission which is about $10^4\,{\rm K}$. In our model the line of sight is binned, and the radiation coefficients are assumed to be constant within a bin. At the front of each bin of length Δs, corresponding to an optical depth $\tau = \Delta s\,\alpha_l$, we find for $\tau > 0$

$$I(\Delta s) = I_0 \exp(-\tau) + \frac{j_c + j_l}{\alpha_l}\,\left[1 - \exp(-\tau)\right] \ , \tag{2}$$

where I_0 is the intensity at the rear boundary.

The change of the intensity across the bin is given by

$$\begin{aligned} \Delta I &= I(\Delta s) - I_0 \\ &= \left(\frac{j_c + j_l}{\alpha_l} - I_0\right)\left[1 - \exp(-\tau)\right] \\ &= \left(\frac{j_c \Delta s + j_l \Delta s}{\tau} - I_0\right)\left[1 - \exp(-\tau)\right] \end{aligned} \tag{3}$$

We are working in the low frequency limit where the brightness temperature T_B is proportional to the intensity. The increment in T_B then is

$$\Delta T_B = \left(\frac{\Delta T_c + \Delta T_l}{\tau} - T_0\right)\,\left[1 - \exp(-\tau)\right] \ , \tag{4}$$

where T_0 is the brightness temperature at the rear boundary of the bin and $\Delta T_c \propto j_c\,\Delta s$ is the increment in continuum brightness temperature along the bin. The increment in the line brightness temperature is given by $\Delta T_l = \tau\,T_{\rm exc}$ where $T_{\rm exc} \propto j_l/\alpha_l$ is the excitation temperature of the atomic-hydrogen gas (see for example section 7.4.1 of Draine (2011)).

For each velocity bin and line of sight, we successively apply eq. 4 to find the radiation temperature at Earth, from which we subtract the continuum temperature to obtain line spectra,

$$T_l = -T_c + \sum_i \Delta T_B(s_i) \ , \quad T_c = \sum_i \Delta T_c(s_i) \ , \tag{5}$$

where T_l is the observed line brightness temperature. Matching those spectra to the observed line spectra will yield ΔT_l for each distance bin. The corresponding contribution to the column density of gas, N_H, is

$$\Delta N_H = (1.8 \cdot 10^{18}\ {\rm s\,K^{-1}\,cm^{-2}\,km^{-1}})\,\Delta v\,\Delta T_l \ , \tag{6}$$

where Δv is the bin width in velocity space.

We use data from the H*I*4PI survey (HI4PI Collaboration et al. 2016), that outperforms the Leiden-Argentina-Bonn survey in angular resolution (16.2′ FWHM), sensitivity ($\sigma_{\rm rms} \simeq 43$ mK), and by its full spatial sampling. Our data cube has an angular sampling of $\Delta l = \Delta b = 5'$ and a velocity binning of $\Delta v \simeq 1.3$ km/s.

2.2. *Continuum Modelling*

[1] https://fermi.gsfc.nasa.gov/ssc/data/access/lat/BackgroundModels.html

The continuum modelling was performed as follows: We have the CHIPASS[2] (Calabretta et al. 2014) and Stockert[3] (Testori et al. 2001; Reich et al. 2001) continuum datasets.

The CHIPASS data were reprojected to match the Stockert data. Missing regions in the CHIPASS data were patched with the Stockert data using a tanh based modulating function to smoothly combine the two data sets. We then fitted a model of the continuum emission consisting of three Gaussian disk components,

$$\Delta T_c/\Delta s = \sum_{i=1}^{3} a_i \exp\left[-\frac{1}{2}\left(\frac{r^2}{\sigma_{r,i}^2}+\frac{z^2}{\sigma_{z,i}^2}\right)\right] \quad (7)$$

where a_i, $\sigma_{r,i}$, and $\sigma_{z,i}$ were the fitted model parameters. The model was fitted in Galaxy-centered cylindrical coordinates with radius, r, and height above the Galactic plane, z. Using least-squares optimization on a ROI of $|l| < 50°$, $|b| < 25°$, we fitted one disk, then fixed that and fitted a second one. We then fixed those two components and fitted a third component initialized to around the GC intense region's extent. Then we freed all parameters to fit the three components simultaneously. The best fit parameters are shown in Table 1.

Using this three-Gaussians model, we created an instance of the model on the grid of the gas-deconvolution cube and renormalized it to the observed continuum temperature for each line of sight, and so the signal in the bins sums up to the observed continuum brightness. As the model is just a simple three-component model, the continuum cube has a few stark point-source-like components when renormalized, which manifest themselves as bright streaks through slices of the cube. The Galactic center is a hotspot in continuum brightness with $T_c \gtrsim 500\,\mathrm{K}$. Figure 1 displays the distribution of continuum emissivity per distance bin, which likewise has a sharp peak at the Galactic center.

2.3. *Algorithm*

For each bin in velocity space in which the modulus of the signal exceeds 0.15 K, we find the eight best-fitting distance solutions in distance bins of 50 pc. The signal is then distributed over those distance solutions using weights that are calculated as in Macias et al. (2018).

Tests show that the nonlinearity in the radiation transport very much complicates accounting for a finite width of the signal from individual clouds and correlations between neighboring lines of sight, at least compared to a Bayesian inference of CO line data (Mertsch & Vittino 2020). To avoid artefacts and a strong dependence on priors we treat each line of sight and velocity bin independently. As we ignore proper motion of gas clouds relative to the local average flow, there is more signal without distance solution than with the deconvolution technique of Pohl et al. (2008). This signal is placed according to the distance solutions at the closest velocity covered in the gas-flow model, but the radiation transport is separately calculated for each velocity bin. Then the distance resolution is reduced by a factor two by combining neighboring distance bins. This fixes the line-of-sight distribution of the signal.

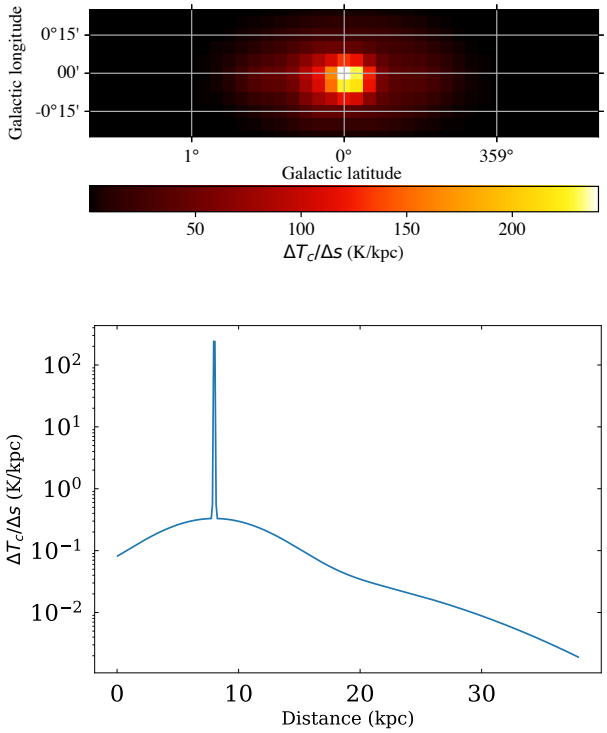

Figure 1. Continuum emission model. Top: Cross section of $\Delta T_c/\Delta s$ at a distance of 8 kpc from the solar system. Bottom: Profile of $\Delta T_c/\Delta s$ for $l = 0°$ and $b = 0°$.

To determine the amplitude of the signal we create a set of 60 logarithmically spaced model signals with integrated line emissivity, $\int ds\, j_l$, ranging from 0.15 K to more than 10^3 K, for which we solve eq. 5. We then search for the one model temperature, T_l, that best matches the observed brightness as given in the HI4PI data. If the observed value is beyond the range of model values, we pick the closest one, otherwise we use linear interpolation between the two nearest models. The rms deviation between model and observed spectrum is computed and retained as accuracy parameter to the model file. In Fig. 2 we display the mean mismatch as a func-

[2] https://lambda.gsfc.nasa.gov/product/foreground/fg_chipass_info.cfm
[3] https://lambda.gsfc.nasa.gov/product/foreground/fg_stockert_villa_info.cfm

Table 1. Best fit parameter values for the three-disk continuum model.

Parameter	Amplitude (a)	Radial standard deviation (σ_r)	Vertical standard deviation (σ_z)
Units	K/kpc	kpc	kpc
Disk 1	0.29	12	5.2
Disk 2	3100	0.038	0.021
Disk 3	1.5	4.0	0.13

NOTE— The a parameters in Eq. 7 were fitted so that after line-of-sight integration in any direction one obtains the brightness temperature. Hence the units of a are K/kpc.

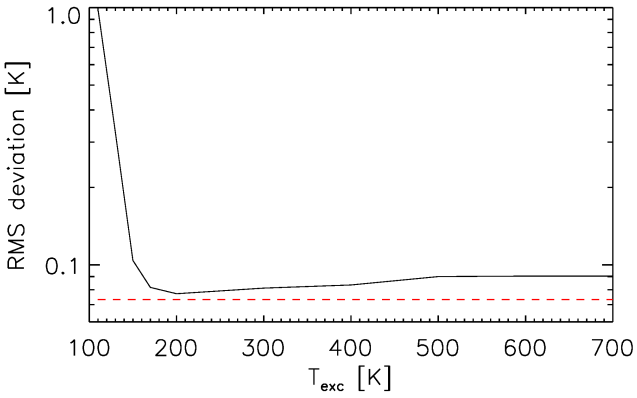

Figure 2. Averaged difference between the model spectra and the observed spectra, plotted as a function of excitation temperature, $T_{\rm exc}$. The red dashed line indicates the mismatch level for an excitation temperature that is allowed to vary with longitude, l and latitude, b.

tion of the excitation temperature, $T_{\rm exc}$. Averaged over the area of interest, we see the smallest deviation with $T_{\rm exc} = 200\,{\rm K}$, and somewhat higher temperatures work nearly as well.

Note that we place gas seen in absorption also on the far side, although it does not provide much absorption there because it is likely behind the continuum source. Otherwise we would construct a near-heavy Galaxy in regions of high absorption.

Figure 3 presents for two values of the excitation temperature, $T_{\rm exc}$, the modelled and observed HI spectra for the line of sight toward the Galactic Center and a second area with high line intensity. To be noted from the top panel of the figure is that solving the radiation transport equation with continuum emission can reproduce strong absorption features and provide an estimate of the HI column density where absorption occurs. Modelling negative line intensity becomes difficult for higher values of $T_{\rm exc}$, in particular for velocities for which the distance solutions are predominantly behind the region of high continuum emissivity. Whereas for $T_{\rm exc} = 200\,{\rm K}$ that happens in only a narrow band around $v = 50\,{\rm km\,s^{-1}}$,

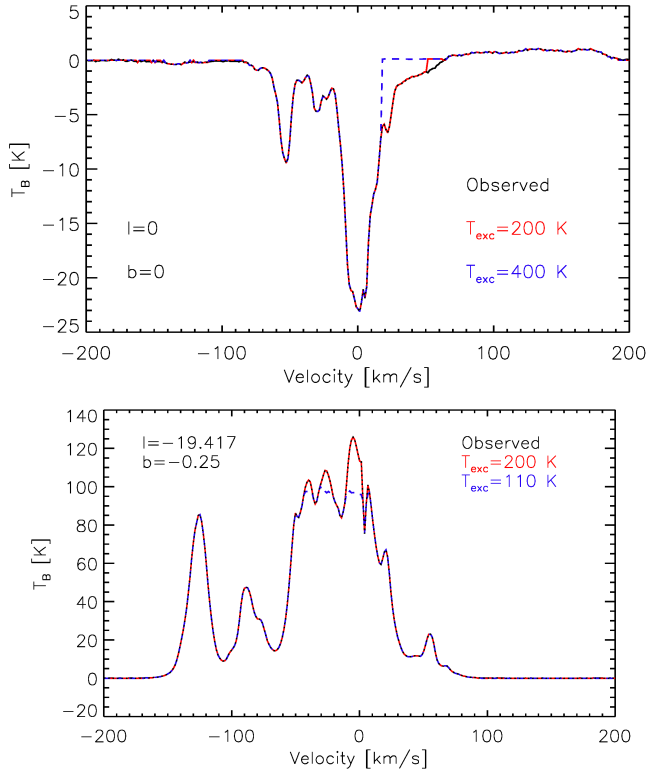

Figure 3. Comparison of the observed and the modelled HI spectrum toward the Galactic Center (top panel) and a line of sight with a high-intensity peak (bottom panel).

implying that only a small fraction of the gas is poorly modelled, a larger mismatch is seen for $T_{\rm exc} = 400\,{\rm K}$.

The signal at $(l, b) = (0°, 0°)$ in the top panel is almost perfectly fit by $T_{\rm exc} = 110{\rm K}$ but that excitation temperature doesn't work well for other lines of sight with high intensity peaks, an instance of which is shown in the bottom panel.

In reality one should expect to find gas clouds on the line of sight that have different excitation temperatures. It is quite conceivable that the absorption feature around $v = 50\,{\rm km\,s^{-1}}$ in the top panel of figure 3 is caused by relatively little cold gas immediately in front of the

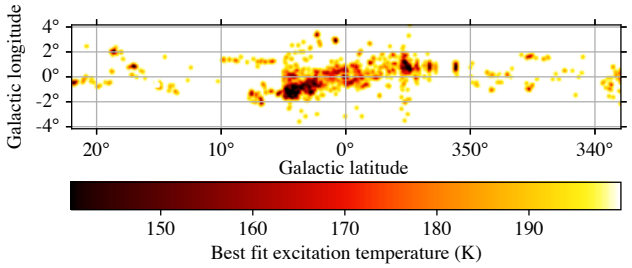

Figure 4. Best-fit excitation temperature for each line of sight. The image was smoothed with a 0.08° Gaussian filter and cropped to contain 99.5% of intensity values for display purposes.

Galactic Center, whereas most of the gas clouds have temperatures of a few hundred Kelvin. We find it impossible to account for variations in the excitation temperature along the line of sight, without introducing a large number of free parameters that are poorly, if at all, constrained. Hence the decision to use a uniform excitation temperature for a particular line of sight. In Fig. 4 we show a map of the best-fit $T_{\rm exc}$ as a function of l and b. Only $|b| \leq 4°$ is shown, as higher latitude areas in our region of interest almost all had $T_{\rm exc} = 200K$.

3. RESULTS

In the previous sections, we presented our improved model for the distribution of HI in the Galaxy. The new templates trace gas in both emission and absorption, and account for negative line intensity. Additionally, we have upgraded the dust correction maps with the use of PLANCK data, but we emphasize that the molecular hydrogen maps in this work are still the same as those in Macias et al. (2018). Likewise, the fit parameters for the cosmic-ray spectra, and hence the gamma-ray emissivity are still considered constant in annuli in galactocentric radius. For comparison, we display in Fig. 5 as a function of l and b the HI column density that is attributed to four of these annuli. The new model, shown on the right, has considerably fewer artefacts than has the older model. An example is the signal at $b \approx 12°$ in the 8-10 kpc annulus that is no longer visible, here on account of a slightly modified treatment of signal beyond the range of Doppler shifts that the model provides. To be noted is the enhanced column density attributed to the Galactic plane at $r \leq 3.5$ kpc, where HI absorption is particularly strong. Within a few degrees from the Galactic Center, this signal is not simply taken from any of the other annuli. Instead it results from the proper modelling of HI absorption and the strong continuum emission from that direction.

In this section, we perform fits to gamma-ray data from the GC region in order to evaluate the impact of

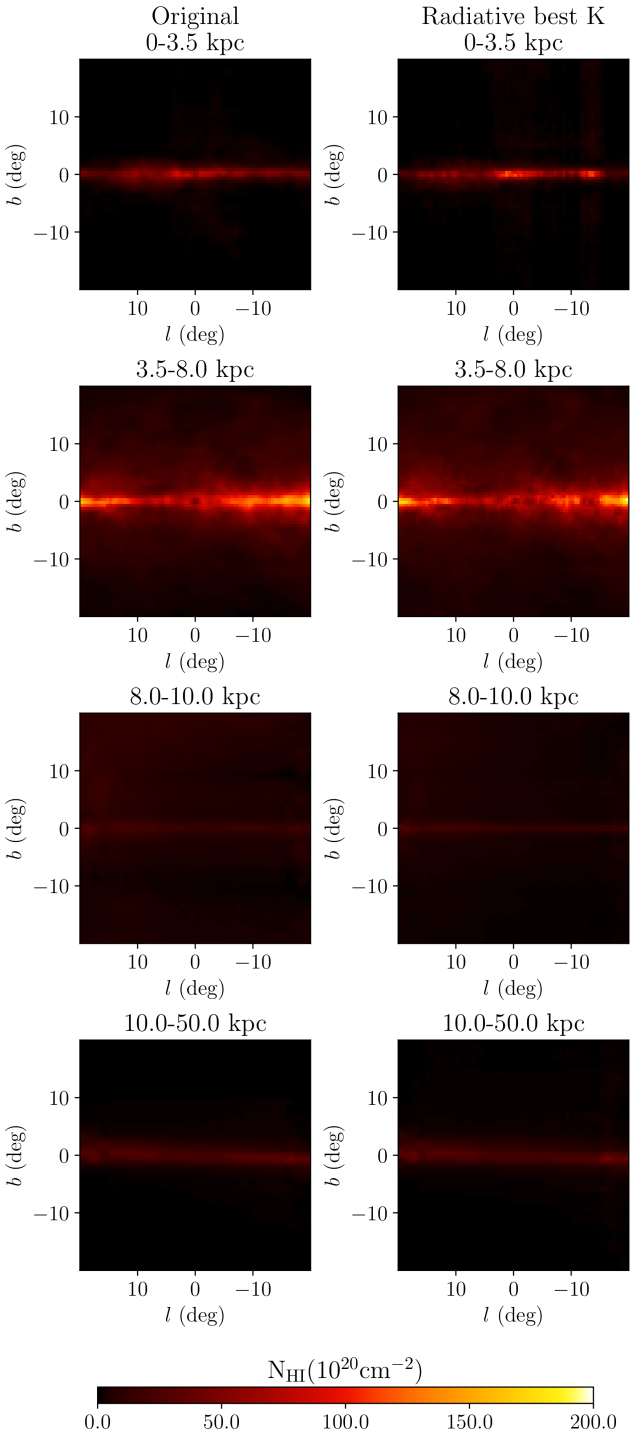

Figure 5. Column density maps for four annuli. The right panels show models that account for continuum emission, and the left panels display models that do not.

the new templates on the characteristics of the GCE. We used eight years (August 4, 2008−August 2, 2016) of PASS 8 RELEASE 3 (P8R3) ULTRACLEANVETO class photon data in the energy range 667 MeV−158 GeV. Details about the data selection cuts, statistical

Baseline model	Additional source	ΔTS	Significance
Basel.	Cored ellips.	0.0	0.0 σ
Basel.	Cored	0.1	0.0 σ
Basel.	BB	282.2	15.3 σ
Basel.	NFW ellips.	647.2	24.2 σ
Basel.	NFW	807.1	27.3 σ
Basel.	NB	1728.9	40.8 σ
Basel.+NB	Cored ellips.	0.1	0.0 σ
Basel.+NB	Cored	0.7	0.0 σ
Basel.+NB	NFW ellips.	1.0	0.0 σ
Basel.+NB	NFW	3.4	0.2 σ
Basel.+NB	BB	261.0	14.7 σ
Basel.+NB+BB	NFW ellips.	0.1	0.0 σ
Basel.+NB+BB	Cored ellips.	0.4	0.0 σ
Basel.+NB+BB	Cored	0.7	0.0 σ
Basel.+NB+BB	NFW	2.6	0.1 σ

Table 2. Statistical significance of the GCE templates for the H*I* maps with varying $T_{\rm exc}$. The base model comprises the new hydrodynamic gas maps introduced in this work (divided in four rings), dust correction maps, inverse Compton maps, the 4FGL point sources, and templates for the Fermi Bubbles, Sun, Moon, Loop I, and isotropic emission (see Appendix C). Additional sources considered in the analysis are: Nuclear bulge (NB) (Nishiyama et al. 2013), boxy bulge (BB) (Coleman et al. 2020), NFW profile with $\gamma = 1.2$, cored dark matter (Read et al. 2016), and ellipsoidal versions of these (see Fig. 3 in (Abazajian et al. 2020)).

procedure, and all other astrophysical templates considered in the region of interest (ROI) model are given in the Appendix.

3.1. *Implications for the GCE*

To evaluate the impact of the new gas maps on the GCE, we include in our baseline model the H*I* maps that best reproduce the observed line emission, namely those with $T_{\rm exc}$ varying as a function of l and b. Similar tests for the best-fitting constant excitation temperature ($T_{\rm exc} = 200$ K) are presented in Appendix C. In addition, the baseline model includes positive and negative dust correction templates (Abdollahi et al. 2020), 3D inverse Compton (IC) maps divided in six rings (Porter et al. 2017), the Fourth Fermi Catalogue (4FGL) of point sources (Abdollahi et al. 2020), a Fermi Bubbles (FB) template (Macias et al. 2019) based on that reconstructed in Ackermann et al. (2014), specialized templates for the Sun and Moon, an isotropic emission model, and a geometrical template for Loop I (see Appendix C).

We first start by running the bin-by-bin procedure, described in Appendix B, with the baseline model. This is done by varying the flux normalization of all the point sources and extended templates such that the log-likelihood is independently maximized in each energy bin, using the *Fermi* PYLIKELIHOOD tool[4]. The next step consists of implementing the bin-by-bin method with an augmented model that includes the GCE templates. We consider four classes of dark matter (DM) profiles, and two maps tracing the distribution of stars in the inner Galaxy (all described in Appendix C). The statistical significance for each new source is obtained by computing the ΔTS as shown in Eq. 2.5 of Macias et al. (2019), and noting that each additional template has 15 degrees of freedom. We stress that when computing the statistical significance of each of the GCE templates, we simultaneously vary the fluxes of the baseline and additional templates. We show the results of this step in the first six rows of Table 2, where the GCE templates are sorted according to their statistical significance.

The fact that some of the additional templates are found with such a high statistical significance suggests that the Baseline model alone is insufficient to explain the data. We thus follow the hierarchical statistical procedure introduced in Macias et al. (2018) to consecutively add to the ROI model the templates with the highest ΔTS. As can be seen in Table 2, using this procedure we find that the data strongly supports the inclusion of the NB template first, and subsequently, the BB template. Importantly, in consistency with previous analyses (e.g., Macias et al. 2018; Bartels et al. 2018; Macias et al. 2019; Abazajian et al. 2020), we find that once the NB and BB templates have been added to the ROI model, the data no longer require any of the DM templates considered in this study.

Compared to our previous articles on this subject, we now find a much greater discriminant power for the GCE templates. Our new study shows that the DM templates are statistically highly disfavoured once the NB template is included in the ROI model (see rows 7-11 in Table 2). To be noted from this table is that while the DM templates are strongly disfavoured, the BB template is detected at very high significance (14.7σ). This highlights that our new hydrodynamic gas maps (with varying $T_{\rm exc}$) drastically improve the sensitivity to the spatial morphology of the GCE templates.

3.2. *Comparisons with previous Galactic diffuse emission models*

Macias et al. (2018) demonstrated that the hydrodynamic gas maps introduced in Pohl et al. (2008) give

[4] https://fermi.gsfc.nasa.gov/ssc/data/analysis/scitools/extended/extended.html

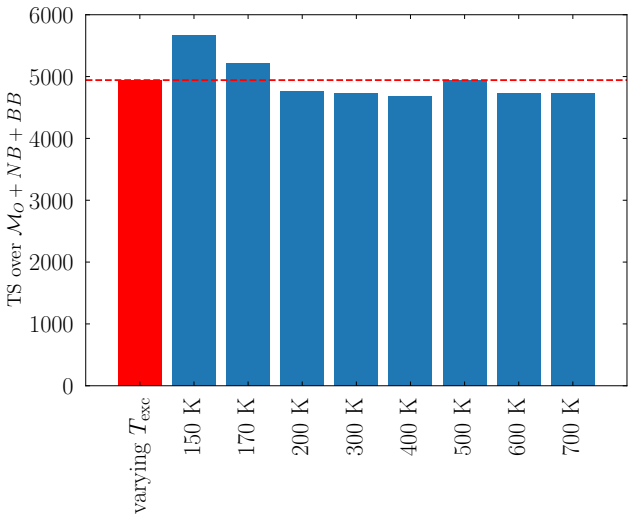

Figure 6. The Test Statistic (TS) of the "Baseline+NB+BB" model in comparison with "Model O + NB+BB" that is based on the previous generation of our hydrodynamic gas maps. The blue bars display the results for H*I* maps with constant $T_{\rm exc}$, and the red bar displays the results for a $T_{\rm exc}$ which varies with l and b. Evidently the new H*I* maps are statistically highly preferred.

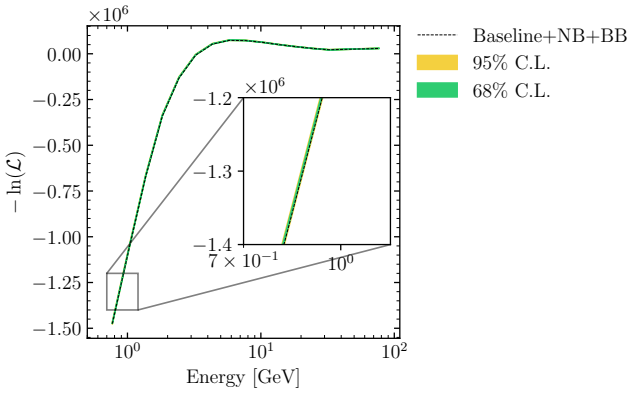

Figure 7. Results of the fit validation tests for our best-fitting model (Baseline+NB+BB), defined in Table 2 and including the H*I* maps with $T_{\rm exc}$ varying with l and b. The black dotted line shows the log-likelihood obtained from the bin-by-bin procedure applied on real data. The green (yellow) band shows the MC expectations at 68% and 95% confidence, respectively, obtained with the same bin-by-bin procedure on Poissonian Monte Carlo simulations of the best-fit 'Baseline+NB+BB' model.

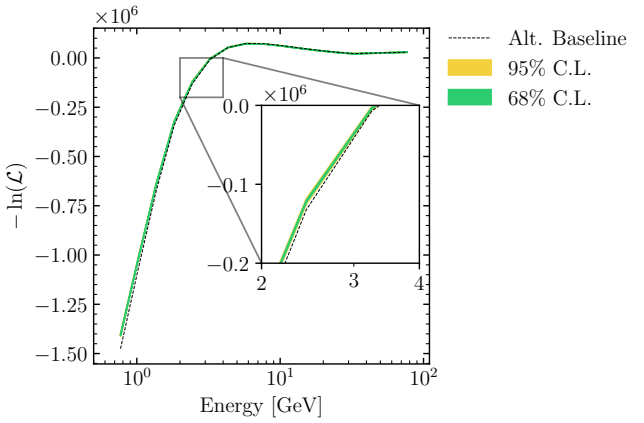

Figure 8. Results a fit validation test applied to an Alternative Baseline model only that includes H*I* maps with $T_{\rm exc} = 150$ K. The validation tests were done using the same method as in Fig. 7. Note that in this case, the NB and BB templates were not included in the fits.

a better fit to the GC data than other gas models in the literature (e.g., Ackermann et al. 2017). The result has been confirmed with a different methodology in Buschmann et al. (2020b) (see e.g., Fig. 3 in that paper).

We now investigate whether our new interstellar gas models provide a better fit to the gamma-ray data than those proposed in Macias et al. (2018). For this comparison, we use the test statistic, TS, defined as $\mathrm{TS} = -2[\ln(\mathcal{L}_1) - \ln(\mathcal{L}_0)]$, where $\mathcal{L}_1$ and $\mathcal{L}_0$ are the likelihood for the "Baseline+NB+BB" model (see Table 2), and the "Model O + NB+BB" model, respectively. Note that "Model O" ($\mathcal{M}_O$) assumes the hydrodynamical H*I* maps introduced in Macias et al. (2018), but is otherwise the same as that in the present study.

Figure 6 displays the results of this analysis. Remarkably, all new H*I* maps are found to have TS values in excess of 4500, and we conclude that our new gas models fit the data significantly better than the previous generation of hydrodynamic gas models (Macias et al. 2018, 2019; Buschmann et al. 2020b). Even though the H*I* maps with $T_{\rm exc} = 150$ K and 170 K seem to be preferred by the gamma-ray data, they do a poorer job at explaining the radio data (see Fig. 2). Our approach in this study was to select the H*I* maps which fit the radio data best. These correspond to the H*I* maps with $T_{\rm exc}$ varying with l and b. We leave for a future investigation to perform a global fit in which we simultaneously fit the radio and gamma-ray data in order to find out the best-fitting excitation temperature $T_{\rm exc}$ for each line of sight.

3.3. *Fit validations*

In Sec. 3.1, we established that the "Baseline+NB+BB" model provides the best fit for our ROI. We now assess whether or not this model is appropriate in an absolute sense, using a similar method to that introduced in Buschmann et al. (2020b). First, we Monte-Carlo (MC) simulate 50 data sets, each with 15 bands, drawn from the "Baseline+NB+BB" model—assuming the data are Poisson distributed. Second, we subject

these synthetic data sets to exactly the same bin-by-bin fitting procedure as was used on real data. Hence the number of degrees of freedom in the fits to MC data is the same as on real data, and so is the expected distribution of the log-likelihood values.

We present the results of the fit validation in Fig. 7. The MC expectations are shown at the 68% (95%) C.L. Importantly, the log-likelihood values obtained from real data conform with the MC expectations. The fact that the best-fitting model "Baseline+NB+BB" passes this important test gives further credence to our method of separating DM models from those of astrophysical origin based on their spatial morphologies.

For comparison purposes, we also performed this same kind of validation test to an "Alternative Baseline" model. This model is defined by substituting the spatially-varying $T_{\rm exc}$ HI maps with those that assume $T_{\rm exc} = 150$ K throughout the Galaxy. Notice that for this test, we did not include the NB and BB templates. The results of this exercise are displayed in Fig. 8. Similarly to what was shown in Fig. 17 of Buschmann et al. (2020b), we find that for $E \gtrsim 4$ GeV the "Alternative Baseline" matches the data at the level of the MC expectations. However, as can be seen, this is not the case for $E \lesssim 4$ GeV. The most likely explanation for this observation is that the data require the inclusion of the NB+BB templates into the ROI model.

3.4. *Gamma-ray Residuals*

It is interesting to inspect the residual images for our best-fitting "Baseline+NB+BB" model. Figure 9 shows the fractional residuals, (Data−Model)/Model, in three different macro energy bins: $[0.6, 1.1]$, $[1.1, 2.8]$ and $[2.8, 11.8]$ GeV. They are constructed by joining various micro energy bins, in which the actual fits are performed and that are narrow enough for a reasonable accuracy of our assumption of a flat gamma-ray spectrum in each bin. The mismatch between model and data is mostly at the $\lesssim 10\%$ level, although we also observe localized correlated residuals that reach up to $20 - 30\%$. These localized residuals are found mostly for latitudes $|b| \gtrsim 8^\circ$ where the GCE is less significant and imperfections in the current FB template would leave their signature.

We note that passing the fit validation tests shown in the previous section is a necessary, but not sufficient condition to be able to claim that the "Baseline+NB+BB" model is a good-fitting model in an absolute sense. Figure 9 shows that our ROI model still requires some further improvements. One possible cause for these localized residuals is that they may be due to sub-threshold point sources in the 4FGL catalog which become more statistically significant with our new HI maps. Even though our current astrophysical model for the GC region is not perfect, the fit validation tests do show that the statistical results obtained in our analysis are very robust.

4. CONCLUSIONS

We devised a new model of the Galactic distribution of atomic hydrogen, HI, that traces gas both in emission and in absorption. For that purpose, we constructed a model of continuum emissivity in the 21-cm waveband that reproduces the continuum brightness observed from the inner Galaxy with the CHIPASS survey (Calabretta et al. 2014). We then solved the radiation transport integral for HI line emission in the presence of continuum radiation for each line of sight and Doppler shift, for which the HI4PI survey reports a non-zero line signal. The mapping of Doppler shift to distance along the line of sight is performed using the gas-flow model of Bissantz et al. (2003) and the algorithm described in Pohl et al. (2008) that provide distance resolution also toward the Galactic Center.

Our explicit radiation-transport modelling can reproduce the negative line signals that one often finds within a few degrees off the Galactic Center. Atomic gas seen in absorption can thus be accounted for. We find an enhanced column density attributed to the Galactic plane at $r \leq 3.5$ kpc, where HI absorption is particularly strong. Within a few degrees off the Galactic Center, this signal is not simply taken from other locations on the line of sight. Instead it results from the proper modelling of HI absorption and the strong continuum emission from that direction.

We test various values of the hydrogen excitation temperature, $T_{\rm exc}$, ranging from 130 K to 700 K. The lower the excitation temperature, the easier it is to reproduce absorption features in the spectra, in particular negative line signals. At the same time, one cannot model line signal with brightness temperatures exceeding $T_{\rm exc}$, and in the presence of continuum emission the achievable line brightness can be well below this limit. For a constant excitation temperature, we find that the HI4PI spectra are best reproduced for $T_{\rm exc} = 200$ K with an average mismatch below 0.08 K or about twice the survey sensitivity. The mismatch increases slowly for higher excitation temperatures and does so quite rapidly for $T_{\rm exc} \lesssim 170$ K. We also constructed a model of the Galactic distribution of atomic hydrogen, in which we allowed $T_{\rm exc}$ to vary as a function of l and b. This model fits the line data best and serves as a fiducial model for the subsequent analysis of the diffuse gamma-ray emission from the inner Galaxy.

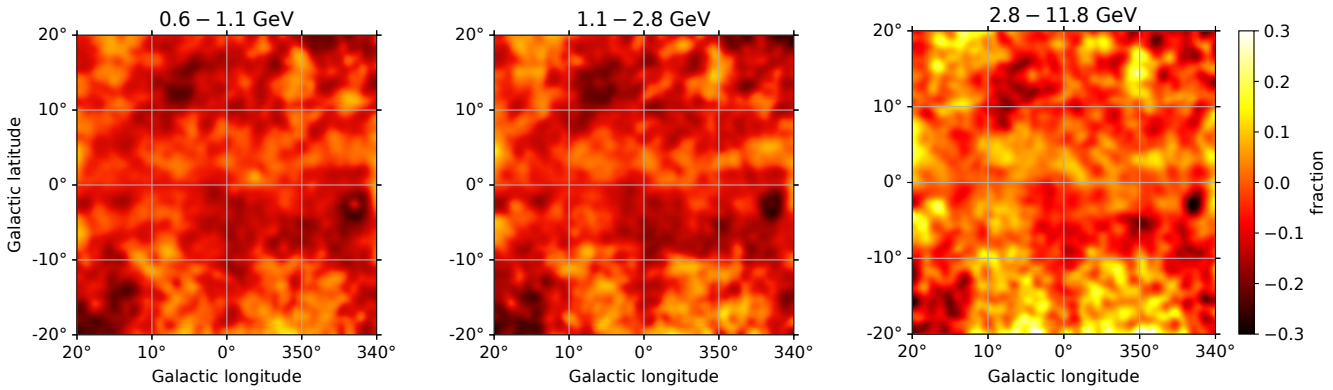

Figure 9. The fractional residuals, (Data-Model)/Model, for the "Baseline+NB+BB" model. Detailed descriptions of the templates included in the ROI model can be found in Appendix C, likewise the gamma-ray spectrum for the "Baseline+NB+BB" model. The images have been smoothed with a Gaussian filter of radius 0.6°.

We then updated our model of the diffuse gamma-ray emission from the inner Galaxy (Macias et al. 2018) with the new maps of Galactic atomic hydrogen and new templates for the dust correction. The model comprises components that describe cosmic-ray induced gamma-ray emission, large-scale features like the Fermi bubbles, a nuclear bulge and a boxy bulge, and minor aspects like the Sun and the Moon. The new H*I* map affects the cosmic-ray induced gamma-ray emission through hadronic interactions and nonthermal bremsstrahlung. We find with high significance, $\Delta\mathrm{TS} \approx 5000$, a much better fit to the diffuse gamma-ray emission from the inner $40^\circ \times 40^\circ$ of the Galaxy as observed with the *Fermi*-LAT, if our new H*I* model is used. A similar improvement in fit quality is seen for all choices of $T_{\rm exc}$ that we probed. The likelihood fit still requires that templates for the nuclear bulge (Nishiyama et al. 2013) and the boxy bulge (Coleman et al. 2020) are included in the model, as was the case in earlier analyses. Already without the boxy bulge, but also with it, there is no evidence whatsoever for any of the dark-matter scenarios we tested. These include with arbitrary spectral form cuspy and cored dark-matter profiles and ellipsoidal versions thereof.

We performed various checks for potential systematic issues without finding an indication for any. The results appear to be robust. Compared to previous studies, we now find a much greater discriminant power for the templates for the Galactic-Center excess. While the dark-matter templates do not significantly improve the fit, the boxy bulge template is detected at nearly the 15σ level. We conclude that our new hydrodynamic gas maps, allowing $T_{\rm exc}$ to vary as a function of l and b, not only provide an unprecedented reconstruction of H*I* line spectra, but also drastically improve the sensitivity to the spatial morphology of the various components of diffuse Galactic gamma-ray emission for the much-discussed Galactic-Center excess.

We foresee that our new H*I* maps will be very useful for the ambitious GC survey program of the forthcoming Cherenkov Telescope Array (Acharyya et al. 2021) and particularly for characterizing the high-energy tail of the GCE at TeV-scale energies (Song et al. 2019; Macias et al. 2021).

5. ACKNOWLEDGMENTS

We thank Shin'ichiro Ando, Roland M. Crocker, and Shunsaku Horiuchi for fruitful discussions. O.M. is supported by the GRAPPA Prize Fellowship.

REFERENCES

Abazajian, K. N., Canac, N., Horiuchi, S., & Kaplinghat, M. 2014, PhRvD, 90, 023526, doi: 10.1103/PhysRevD.90.023526

Abazajian, K. N., Horiuchi, S., Kaplinghat, M., Keeley, R. E., & Macias, O. 2020, PhRvD, 102, 043012, doi: 10.1103/PhysRevD.102.043012

Abdollahi, S., Acero, F., Ackermann, M., et al. 2020, ApJS, 247, 33, doi: 10.3847/1538-4365/ab6bcb

Acharyya, A., Adam, R., Adams, C., et al. 2021, JCAP, 2021, 057, doi: 10.1088/1475-7516/2021/01/057

Ackermann, M., Albert, A., Atwood, W. B., et al. 2014, ApJ, 793, 64, doi: 10.1088/0004-637X/793/1/64

Ackermann, M., Ajello, M., Albert, A., et al. 2017, ApJ, 840, 43, doi: 10.3847/1538-4357/aa6cab

Baba, J., Saitoh, T. R., & Wada, K. 2010, PASJ, 62, 1413, doi: 10.1093/pasj/62.6.1413

Bartels, R., Krishnamurthy, S., & Weniger, C. 2016, Phys. Rev. Lett., 116, 051102, doi: 10.1103/PhysRevLett.116.051102

Bartels, R., Storm, E., Weniger, C., & Calore, F. 2018, Nature Astronomy, 2, 819, doi: 10.1038/s41550-018-0531-z

Bissantz, N., Englmaier, P., & Gerhard, O. 2003, MNRAS, 340, 949, doi: 10.1046/j.1365-8711.2003.06358.x

Buschmann, M., Rodd, N. L., Safdi, B. R., et al. 2020a, Phys. Rev. D, 102, 023023, doi: 10.1103/PhysRevD.102.023023

—. 2020b, PhRvD, 102, 023023, doi: 10.1103/PhysRevD.102.023023

Calabretta, M. R., Staveley-Smith, L., & Barnes, D. G. 2014, PASA, 31, e007, doi: 10.1017/pasa.2013.36

Calore, F., Donato, F., & Manconi, S. 2021, arXiv e-prints, arXiv:2102.12497. https://arxiv.org/abs/2102.12497

Chang, L. J., Mishra-Sharma, S., Lisanti, M., et al. 2020, Phys. Rev. D, 101, 023014, doi: 10.1103/PhysRevD.101.023014

Chrobáková, Ž., López-Corredoira, M., Sylos Labini, F., Wang, H. F., & Nagy, R. 2020, A&A, 642, A95, doi: 10.1051/0004-6361/202038736

Coleman, B., Paterson, D., Gordon, C., Macias, O., & Ploeg, H. 2020, Mon. Not. Roy. Astron. Soc., 495, 3350, doi: 10.1093/mnras/staa1281

Di Mauro, M. 2021, PhRvD, 103, 063029, doi: 10.1103/PhysRevD.103.063029

Draine, B. T. 2011, Physics of the Interstellar and Intergalactic Medium

Gibson, S. J., Taylor, A. R., Higgs, L. A., Brunt, C. M., & Dewdney, P. E. 2005, ApJ, 626, 214, doi: 10.1086/429871

Gordon, C., & Macías, O. 2013, PhRvD, 88, 083521, doi: 10.1103/PhysRevD.88.083521

Grenier, I. A., Casandjian, J.-M., & Terrier, R. 2005, Science, 307, 1292, doi: 10.1126/science.1106924

HI4PI Collaboration, Ben Bekhti, N., Flöer, L., et al. 2016, A&A, 594, A116, doi: 10.1051/0004-6361/201629178

Hooper, D., & Goodenough, L. 2011, Physics Letters B, 697, 412, doi: 10.1016/j.physletb.2011.02.029

Jóhannesson, G., Porter, T. A., & Moskalenko, I. V. 2018a, ApJ, 856, 45, doi: 10.3847/1538-4357/aab26e

—. 2018b, ApJ, 856, 45, doi: 10.3847/1538-4357/aab26e

Leane, R. K., & Slatyer, T. R. 2019, arXiv e-prints, arXiv:1904.08430. https://arxiv.org/abs/1904.08430

—. 2020a, Phys. Rev. D, 102, 063019, doi: 10.1103/PhysRevD.102.063019

—. 2020b, PhRvL, 125, 121105, doi: 10.1103/PhysRevLett.125.121105

Lee, S. K., Lisanti, M., Safdi, B. R., Slatyer, T. R., & Xue, W. 2016, Phys. Rev. Lett., 116, 051103, doi: 10.1103/PhysRevLett.116.051103

List, F., Rodd, N. L., & Lewis, G. F. 2021, arXiv e-prints, arXiv:2107.09070. https://arxiv.org/abs/2107.09070

Macias, O., & Gordon, C. 2014, PhRvD, 89, 063515, doi: 10.1103/PhysRevD.89.063515

Macias, O., Gordon, C., Crocker, R. M., et al. 2018, Nature Astronomy, 2, 387, doi: 10.1038/s41550-018-0414-3

Macias, O., Horiuchi, S., Kaplinghat, M., et al. 2019, JCAP, 2019, 042, doi: 10.1088/1475-7516/2019/09/042

Macias, O., van Leijen, H., Song, D., et al. 2021, MNRAS, 506, 1741, doi: 10.1093/mnras/stab1450

Mertsch, P., & Vittino, A. 2020, arXiv e-prints, arXiv:2012.15770. https://arxiv.org/abs/2012.15770

Mishra-Sharma, S., & Cranmer, K. 2021, arXiv e-prints, arXiv:2110.06931. https://arxiv.org/abs/2110.06931

Nishiyama, S., Yasui, K., Nagata, T., et al. 2013, ApJ. Lett., 769, L28. http://stacks.iop.org/2041-8205/769/i=2/a=L28

Pettitt, A. R., Dobbs, C. L., Acreman, D. M., & Price, D. J. 2014, MNRAS, 444, 919, doi: 10.1093/mnras/stu1075

Planck Collaboration, Aghanim, N., Ashdown, M., et al. 2016, A&A, 596, A109, doi: 10.1051/0004-6361/201629022

Pohl, M., Englmaier, P., & Bissantz, N. 2008, ApJ, 677, 283, doi: 10.1086/529004

Porter, T. A., Jóhannesson, G., & Moskalenko, I. V. 2017, ApJ, 846, 67, doi: 10.3847/1538-4357/aa844d

Read, J. I., Agertz, O., & Collins, M. L. M. 2016, Mon. Not. Roy. Astron. Soc., 459, 2573, doi: 10.1093/mnras/stw713

Reich, P., Testori, J. C., & Reich, W. 2001, A&A, 376, 861, doi: 10.1051/0004-6361:20011000

Sofue, Y. 2015, PASJ, 67, 75, doi: 10.1093/pasj/psv042

Song, D., Macias, O., & Horiuchi, S. 2019, PhRvD, 99, 123020, doi: 10.1103/PhysRevD.99.123020

Su, M., Slatyer, T. R., & Finkbeiner, D. P. 2010, ApJ, 724, 1044, doi: 10.1088/0004-637X/724/2/1044

Testori, J. C., Reich, P., Bava, J. A., et al. 2001, A&A, 368, 1123, doi: 10.1051/0004-6361:20010088

Wolleben, M. 2007, Astrophys. J., 664, 349, doi: 10.1086/518711

APPENDIX

A. *FERMI*-LAT DATA SELECTION

We used eight years (August 4, 2008−August 2, 2016) of PASS 8 RELEASE 3 (P8R3) ULTRACLEANVETO class photon data in the energy range 667 MeV−158 GeV. Photons detected at zenith angles $> 90^\circ$ were removed to reduce the contamination from gamma-rays generated by cosmic ray interactions in the Earth's atmosphere. Additionally, we applied the recommended data filters (DATA_QUAL>0)&&(LAT_CONFIG==1).

The data reduction as well as the data analysis were performed with the FERMITOOLS v1.0.1[5] package, and instrument response function P8R3_ULTRACLEANVETO_V2. The ROI of the analysis is defined by a square region of size $40^\circ \times 40^\circ$ centered at Galactic coordinates $(l, b) = (0, 0)$. Moreover, we used a binned-likelihood method with a spatial binning of 0.2°, and 15 logarithmically-spaced energy bins (in the range 667 MeV−158 GeV).

B. GAMMA-RAY ANALYSIS PROCEDURE

We used a similar pipeline to that introduced in Macias et al. (e.g., 2019); Abazajian et al. (e.g., 2020). In particular, we fitted our ROI model (see Appendix C) to the data using a bin-by-bin analysis procedure in which we maximized the likelihood function separately at each individual energy bin. We obtained the bin fluxes for each template by assuming a simple power-law with slope -2, $dN/dE = N_0 E^{-2}$, and varying the bin-wise normalisation N_0 of all the templates in the fits. An advantage of using a bin-by-bin procedure over a broad-band analysis is that, with the former, there is little or no need to make assumptions about the spectral shape of a new template, rather the template spectrum is obtained in a completely data-driven way. We note in passing that the fitting was done with the PYLIKELIHOOD routine, the standard maximum-likelihood method in FERMITOOLS. In our analysis, we used the bin-by-bin method to evaluate the best-fit spectral values, and the statistical significance for each new source added in our ROI model. An advantage of using `Fermitools` for our fits, is that it rigorously accounts for the point spread function of the LAT. In order to evaluate the statistical significance of a new template we compute the ΔTS for the full energy range as shown in Eq. 2.5 of Macias et al. (2019). Note that since the normalization of the sources are varied independently at each energy bin, we need to use the mixture distribution, explained in Macias et al. (2019), to correctly compute the statistical significance of a new source. In doing so, we account for the number of degrees of freedom for a new extended source, which is the same as the number of energy bins.

C. ASTROPHYSICAL TEMPLATES

HADRONIC AND BREMSSTRAHLUNG GAMMA RAYS

The dominant contributions to the gamma-ray emission within our ROI are hadronic and bremsstrahlung emission resulting from the interaction of Galactic cosmic-ray protons and electrons with interstellar gas. Since both of these components are spatially correlated with the distribution of interstellar gas, we model them in a data-driven way. Namely, we include templates of H*I*, H_2, and dust correction maps in our ROI model and then reconstruct their spectra using the bin-by-bin fitting procedure explained in Appendix B. The H_2 maps are the same as those in Macias et al. (2018), whereas the hydrodynamic H*I* and dust correction templates are updated. The ring subdivision of the gas maps allows to account for the radial evolution of cosmic ray density, and the small width of the energy bins permits to recover their respective gamma-ray spectra.

For our baseline model, we selected the hydrodynamic H*I* and dust correction maps denoted as "best $T_{\rm exc}$", as these provide the statistically most favoured model of the line spectra of atomic hydrogen.

DUST CORRECTION TEMPLATES

Molecular hydrogen that is not well mixed with carbon monoxide will not be traced by the CO 2.6 mm emission. Furthermore, assuming a constant atomic hydrogen spin temperature along a particular line of sight can give an incorrect estimate of column density. To correct for these deficiencies we included dust correction templates based on the methods used by Abdollahi et al. (2020)[6]. Infrared thermal emission from dust provides an alternative method of

[5] https://github.com/fermi-lat/Fermitools-conda/wiki

[6] See also https://fermi.gsfc.nasa.gov/ssc/data/analysis/software/aux/4fgl/Galactic_Diffuse_Emission_Model_for_the_4FGL_Catalog_Analysis.pdf.

tracing hydrogen gas in the Milky Way (Grenier et al. 2005). The correction templates are obtained by subtracting the components of the dust emission that are correlated with the gas already traced by 21 cm and 2.6 mm emission.

We applied this method to the Planck dust optical depth map[7]. After subtracting the components of the Planck dust optical depth map that were linearly correlated with our estimated atomic and molecular hydrogen gas maps, the residuals were separated into positive and negative components. The positive residuals physically represent hydrogen that is not traced by the relevant emission, known as the dark neutral medium, or an over estimation of the atomic hydrogen spin temperature. Negative residuals represent an underestimation of the spin temperature. The results are displayed in Fig. 11.

INVERSE COMPTON EMISSION

We similarly need a model for diffuse, inverse Compton (IC) emission, the second largest source of background, and here we choose the six-ring IC model introduced in Abazajian et al. (2020), because it allows to account for modelling uncertainties such as a potential new central source of electron or possible bias introduced by assumptions on the normalization and shape of the interstellar radiation field (ISRF) and the electron injection spectra.

We constructed the IC maps using `GALPROP V56` and the propagation parameter setup SA50, shown in Table 5 of Jóhannesson et al. (2018b). It should be noted that these IC maps are based on 3D models for the ISRF (Porter et al. 2017), and hence they do not need the simplifying assumptions that were required in previous versions of the `GALPROP` code.

LOW-LATITUDE FERMI BUBBLES

The Fermi bubbles (FB) are one of the strongest sources of fore-/background emission in our sky region. The FB are themselves defined as highly statistically significant and spatially coherent gamma-ray residuals, whose spectra are well described by a simple power-law with a relatively hard slope, $s \simeq -1.9$, in the energy range of our analysis (Su et al. 2010; Ackermann et al. 2014). Here, we use an improved version (Macias et al. 2019) of the FB template constructed using a spectral component analysis by the *Fermi* Collaboration (Ackermann et al. 2014).

POINT SOURCES

We modelled gamma-ray point sources using the 4FGL Abdollahi et al. (2020). Specifically, we assumed the release `gll_psc_v20.fit`, which contains 487 gamma-ray point sources in our ROI. Unfortunately, varying the normalization of all these point sources at once in a maximum-likelihood run is very challenging, and so we opted for following the hybrid-modelling procedure implemented in Macias et al. (2019). In particular, we floated the normalization of each of the 120 brightest point sources in our RoI, and for the remaining 367 sources we constructed a point source population template assuming the flux ratios reported in the 4FGL. The population template was included in the fits with its overall normalization free to vary at each energy bin. This is a reasonable simplification given that our data selection cuts are the same as those in the 4FGL.

GCE TEMPLATES

Detailed descriptions of the templates used to model the GCE are given in Appendix B of Abazajian et al. (2020) (and references therein). In summary, we model the GCE signal with maps tracing the distribution of stellar mass in the Galactic bulge, or with maps describing the distribution of Galactic DM. For the bulge stars, we included two independent templates: the "Boxy Bulge" (BB) model proposed in Coleman et al. (2020), and the observational "Nuclear Bulge" (NB) map presented in Nishiyama et al. (2013). For the DM distribution, we used a cuspy profile, given by a Navarro-Frenk-White (NFW) model with slope $\gamma = 1.2$, and a cored profile, given by a Read function with $\gamma = 1.0$ and core radius 1 kpc (Read et al. 2016). Furthermore, we considered ellipsoidal versions of these. For full details of our profile choices see Fig.3 of Abazajian et al. (2020) and text therein.

OTHER STANDARD TEMPLATES

Additional extended sources considered in our analysis include Loop I (Wolleben 2007), maps for the *Sun* and the *Moon* tailor-made for our data selection cuts, extracted from the 4FGL, and an isotropic gamma-ray model (`iso_P8R3_ULTRACLEANVETO_V2_v1.txt`).

[7] COM_CompMap_Dust-GNILC-Model-Opacity_2048_R2.01.fits, Planck Collaboration et al. (2016)

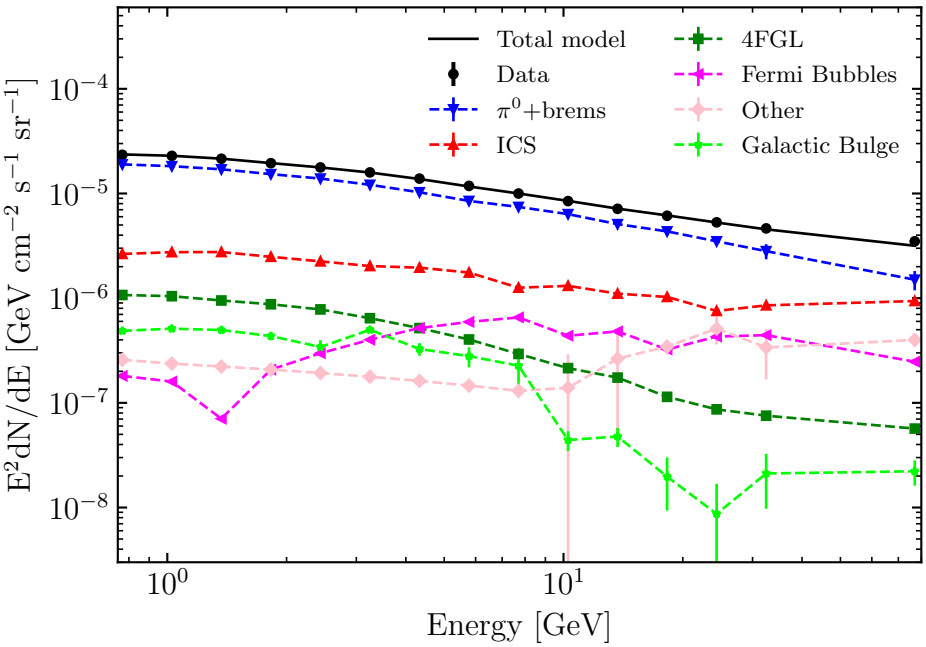

Figure 10. The best-fit spectra for components of the "Baseline+NB+BB" model, cf. Table 2. The Baseline model includes the H*I* maps with $T_{\rm exc}$ varying with l and b, divided in four rings, 3D inverse Compton (IC) maps divided in six rings, the 4FGL catalog of point sources (Abdollahi et al. 2020), the Fermi Bubbles template, specialized templates for the Sun and Moon, an isotropic emission model, and a geometrical template for Loop I (see Appendix C). We have grouped several components together for presentation purposes.

D. GAMMA-RAY SPECTRUM

The spectrum for the best-fitting "Baseline+NB+BB" model (see Table 2) is shown in Fig. 10. As in our previous studies (e.g., Macias et al. 2018, 2019; Abazajian et al. 2020), we find that the fitting procedure produces physically sensible spectra. For simplicity, we have thematically grouped the spectra of different templates. For example, the spectra for the H*I*, CO, and dust maps is displayed as "π^0+bremss", the spectra of all the gamma-ray point sources is shown as one single line denoted "4FGL", and likewise for the rest of the templates of our ROI model.

E. IMPACT OF H*I* SYSTEMATICS ON THE GCE

Previous studies (e.g., Macias et al. 2018; Bartels et al. 2018; Macias et al. 2019; Abazajian et al. 2020) have demonstrated that the GCE signal is better explained by stellar mass templates than DM templates. As stated in the introduction, those studies assumed H*I* maps with a constant excitation temperature through the Galaxy. In contrast, the fiducial H*I* maps included in the main pipeline of the present study consider a excitation temperature which varies with longitude and latitude and accounts for the radiation transport in the presence of continuum emission. In this section, we repeat the hierarchical fitting procedure, whose results are summarized in Table 2, except that this time we replace the fiducial H*I* maps with those for $T_{\rm exc} = 200$ K that among all tested constant excitation temperatures provides the best reproduction of the H*I* line spectra (see Fig. 2).

Table 3 shows the statistical significance for each of the GCE templates for fixed $T_{\rm exc} = 200$ K. To be noted is that they are qualitatively and quantitatively very similar to those obtained with our fiducial ROI model. We again find that the GCE data strongly prefers the stellar-mass templates as a proxy for the GCE morphology. Furthermore, as was found with our Baseline model and with the "Alt. Baseline", we find that in order to remove any support of the DM hypothesis, it is sufficient to add the NB template to the "Alt. Baseline". However, as seen in row 12 of Table 3, the BB template is still required by the data. We thus include the BB template into the sky model and confirm our negative DM results.

Baseline model	Additional source	ΔTS	Significance
Alt. Baseline	Cored ellipsoidal	1.3	0.0 σ
Alt. Baseline	Cored	2.0	0.1 σ
Alt. Baseline	BB	304.2	15.9 σ
Alt. Baseline	NFW ellipsoidal	682.7	24.9 σ
Alt. Baseline	NFW	837.9	27.8 σ
Alt. Baseline	NB	1753.0	41.1 σ
Alt. Baseline+NB	Cored	2.2	0.1 σ
Alt. Baseline+NB	Cored ellipsoidal	2.4	0.1 σ
Alt. Baseline+NB	NFW ellipsoidal	3.5	0.2 σ
Alt. Baseline+NB	NFW	5.7	0.5 σ
Alt. Baseline+NB	BB	283.2	15.3 σ
Alt. Baseline+NB+BB	Cored ellipsoidal	0.1	0.0 σ
Alt. Baseline+NB+BB	NFW ellipsoidal	0.5	0.0 σ
Alt. Baseline+NB+BB	Cored	0.6	0.0 σ
Alt. Baseline+NB+BB	NFW	2.3	0.1 σ

Table 3. Statistical significance of the GCE templates assuming HI maps with $T_{\rm exc} = 200$ K. The "Alternative Baseline" model is the same as that shown in Table 2, except that the fiducial HI maps are replaced with those for a constant excitation temperature, $T_{\rm exc} = 200$ K.

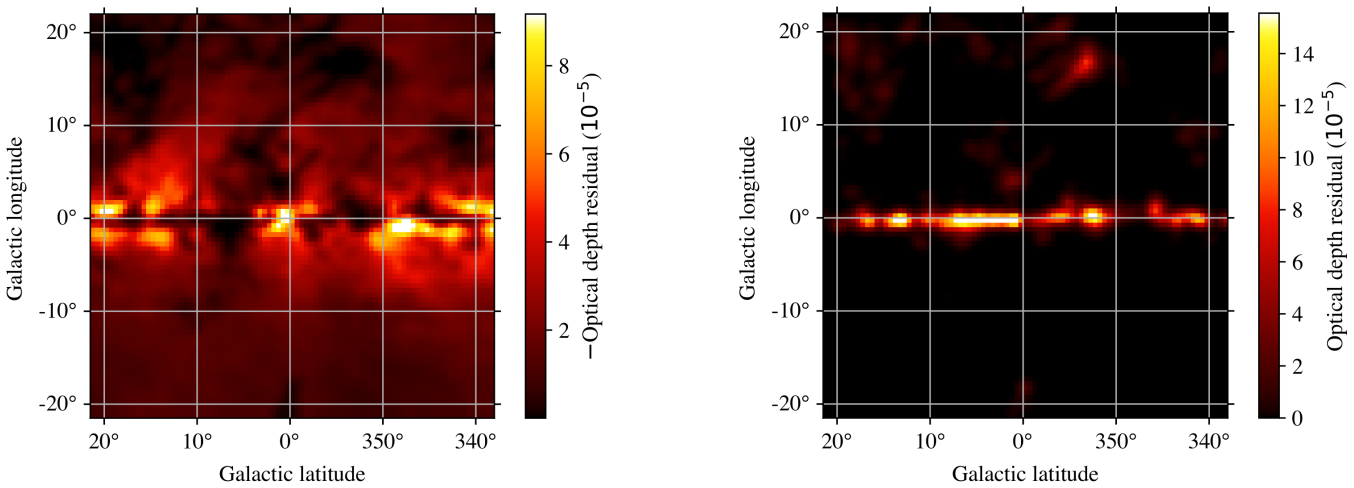

Figure 11. Dust residual maps. On the left we have plotted the negative residuals (multiplied by −1) and on the right the positive residuals. For display purposes the images have been smoothed with a Gaussian filter of radius 0.5°, and the colorbar has been chosen to encompass 99.5% of intensity values.